



Universiteit  
Leiden  
The Netherlands

**Biophysical studies of intracellular and cellular motility**  
Mytiliniou, M.

**Citation**

Mytiliniou, M. (2025, January 16). *Biophysical studies of intracellular and cellular motility*. Retrieved from <https://hdl.handle.net/1887/4176388>

Version: Publisher's Version

License: [Licence agreement concerning inclusion of doctoral thesis in the Institutional Repository of the University of Leiden](#)

Downloaded from: <https://hdl.handle.net/1887/4176388>

**Note:** To cite this publication please use the final published version (if applicable).

## CHAPTER 4

---

# EFFECT OF $G_4C_2$ REPEAT EXPANSIONS ON THE MOTION OF LYSOSOMES INSIDE NEURITES

---

*The  $G_4C_2$  hexanucleotide repeat expansion (HRE) in the *c9orf72* locus is a mutation associated with amyotrophic lateral sclerosis, and recent evidence suggests a link with disrupted axonal trafficking in neurons. Here, using a neuron-like cell line without, or transfected with,  $G_4C_2$  repeats, we characterize the motion of lysosomes inside neurites which were either aligned or oriented randomly on the substrate, implementing time-resolved (local) mean squared displacement (l)MSD analysis and differentiation among sub-diffusive, diffusive, and super-diffusive trajectory parts. Our results suggest that in the presence of the  $G_4C_2$  repeats, lysosome motility is hampered, exhibiting overall decreased MSD and speed, more prominently inside aligned neurites. Moreover, a more prominent effect in the super-diffusive drift velocity and diffusive motion diffusion coefficient was evident when the motion occurred inside aligned neurites. Trajectories which included super-diffusive motion, exhibited a varied ratio of anterograde/retrograde/neutral for both neurite geometries in the presence of  $G_4C_2$  repeats but a similar instantaneous velocity decrease for both directions in each neurite geometry. Our findings support the hypothesis that impaired axonal trafficking emerges in the presence of the  $G_4C_2$  HRE, and demonstrate that this effect is more prominent when the neurites are aligned.*

---

This chapter is based on: **Mytiliniou M.**, Wondergem A.J., Feliksik M., Schmidt T. & Heinrich D.M. "Effect of  $G_4C_2$  Repeat Expansions on the Motion of Lysosomes Inside Neurites", *Submitted*

## 4.1 Introduction

Intracellular homeostasis is intricately regulated and disruptions can contribute to the pathology of various diseases. One critical process for the maintenance of cellular homeostasis is intracellular trafficking, and particularly deficits in axonal transport in neuron cells have been associated with neurodegenerative diseases [1, 2]. The autophagy pathway, a process responsible for the degradation of intracellular components such as aggregated proteins and foreign bodies, entails the fine tuning of a plethora of associated mechanisms, among which, lysosome transport [3]. Both the autophagy pathway in general [4] and the lysosome trafficking specifically [5], have been linked with neurodegenerative diseases pathogenesis.

Amyotrophic lateral sclerosis (ALS) is a devastating, terminal neurodegenerative disease with diverse genetic causes, a multitude of which share a common connection with the autophagy pathway [6]. A mutation in chromosome 9, open reading frame 72 (c9orf72) associated with ALS has been drawing significant attention as it accounts for more ALS cases than any other known ALS-associated mutation [7–9]. The malfunction is caused by a G<sub>4</sub>C<sub>2</sub> hexanucleotide repeat expansion (HRE) in a non-coding region of the c9orf72 locus. Non-affected, healthy individuals have  $n=2-19$  (G<sub>4</sub>C<sub>2</sub>)<sub>n</sub> units, whereas ALS patients have from  $n=24-38$  (G<sub>4</sub>C<sub>2</sub>)<sub>n</sub> repeat units up to hundreds, or even thousands [10–16]. The (G<sub>4</sub>C<sub>2</sub>)<sub>n</sub> expansion is transcribed into RNA, in all six reading frames of the sense and anti-sense direction, forming stable G-quadruplexes or hairpins, which aggregate to RNA foci [16–19]. In addition, all RNA products are translated, via non-ATG initiated (RAN) translation, into non-functional dipeptide-repeat (DPR) proteins: glycine-alanine (GA), glycine-arginine (GR), proline-alanine (PA), proline-arginine (PR) and glycine-proline (GP, generated from both the sense and anti-sense reading frames) [20–27]. Studies which focused on comprehending the normal function of the gene product have revealed that the c9orf72 protein is implicated, among others, with the autophagy-lysosome pathway and with lysosome homeostasis [28, 29]. Moreover, research on the c9orf72 repeat expansion mutation and its associated RNA and DPR protein products demonstrate evidence of disrupted vesicle trafficking [30] and autophagy [31–39], as well as disrupted axonal trafficking of lysosomes [40] and mitochondria [41].

Axonal trafficking is interrelated with, and substantially influenced by, the cytoskeletal organization [42–44], which in turn is affected by the extracellular matrix (ECM). Using a neuronal cell model, we have previously demonstrated that the dimensionality of neurites, which are precursors of dendrites and axons in immature neurons [45], has a distinct effect on lysosome transport, with faster lysosomal motility arising within neurites that are aligned along a line. It was also found that disruption of intracellular homeostasis via sucrose accumulation and induced lysosomal swelling, not only affected each motion mode (sub-diffusive, diffusive or super-diffusive) of these organelles differently,

but was also dependent on the configuration of the neurites within which the motion occurred [46, 47].

Here, we expand upon that previous work, to explore the interplay between organelle transport and the same two neurite geometries with a disease-associated homeostasis disruption. Specifically we investigate whether solely the presence of  $(G_4C_2)$  repeat expansions in the intracellular environment gives rise to defect lysosomal trafficking inside neurites, and the interplay with the neurite dimensionality. To this end, PC12 cells were transfected with plasmids carrying  $(G_4C_2)_{20}$  or  $(G_4C_2)_{39}$ , preceded by a start codon aligned such as to result in the production of  $(GR)_{20}$  or  $(GA)_{39}$ , respectively. The presence of repeats-carrying transcribed RNA was verified via fluorescence signal quantification of single molecule fluorescence in situ hybridization (smFISH). Lysosomes inside neurites of cells carrying the  $G_4C_2$  repeats demonstrated an overall decrease in the mean-squared displacement (MSD) and instantaneous velocity, which was more eminent when the neurites were aligned. This was consistent for all three transport modes, super-diffusive, diffusive, and sub-diffusive, which were analyzed in more detail via local MSD (lMSD). Interestingly, the MSD decline for all transport modes of lysosomes inside aligned neurites was similar for both repeats expansions and more distinct in comparison to randomly oriented neurites, especially for super- and diffusive motion states along with their respective drift velocities and diffusion coefficients. Lastly, for trajectories exhibiting super-diffusive motion, we observed an effect on the ratio of anterograde/retrograde/neutral lysosomal trajectories in the presence of the HRE, which varied for the two neurite geometries, while the repeats-associated decrease of the instantaneous velocity was similar for both directions in each neurite geometry.

## 4.2 Results

### 4.2.1 Neuron-like model system carrying (G<sub>4</sub>C<sub>2</sub>) repeats and dynamic analysis of lysosomal trajectories inside neurites of varying geometry

To characterize the motion of lysosomes in the presence of a disease-associated intracellular homeostasis disruption, namely the (G<sub>4</sub>C<sub>2</sub>)<sub>n</sub> repeat expansion, we transfected PC12 cells with plasmids carrying (G<sub>4</sub>C<sub>2</sub>)<sub>20</sub> or (G<sub>4</sub>C<sub>2</sub>)<sub>39</sub>, preceded by a start codon aligned such as to result in the production of (GR)<sub>20</sub> or (GA)<sub>39</sub>, respectively. Studies have shown that poly-GA is the most abundant of the five DPR protein species in patients [48, 49], and cells [26, 50, 51]. In addition, this DPR protein is very aggregation-prone and has been shown to trigger pathological phenotypes in a zebrafish model [52]. Likewise, arginine-rich DPR proteins, such as the poly-GR, have shown higher expression than other DPR protein species [26] and correlation with pathological phenotypes in patient cells [53], fly model [54], chick embryo [55], *C.elegans* [56], and zebrafish [57]

The presence of repeats-carrying transcribed RNA in the transfected cells was confirmed by quantifying the smFISH fluorescent signal (Fig. S.1). A five-fold increase was observed in the signal of cells transfected with (G<sub>4</sub>C<sub>2</sub>)<sub>20</sub>, as compared with the control case (the auto-fluorescence of the cells), and less than two-fold increase in comparison with the non-specific binding signal of the FISH probes. The increase of the FISH fluorescence intensity in cells transfected with (G<sub>4</sub>C<sub>2</sub>)<sub>39</sub> was less than with (G<sub>4</sub>C<sub>2</sub>)<sub>20</sub>, as compared to both respective controls, which could be attributed to the RNA being more aggregation-prone, thus hindering binding of the FISH probes.

Cell shape can influence intracellular processes, such as the transport of organelles, vesicles and molecules. We have previously shown that the neurite geometry affects lysosomal motility and a sucrose-induced perturbation in the intracellular environment has evident and distinct impact on the motion of lysosomes in the different neurite geometries. Similarly, here, we analyzed the motion of lysosomes inside neurites, which adopted either of two distinct geometries, of PC12 cells without or transfected with plasmids carrying (G<sub>4</sub>C<sub>2</sub>)<sub>20</sub> or (G<sub>4</sub>C<sub>2</sub>)<sub>39</sub>. As described in detail previously [46], the neurites were either guided to stretch along chemically-patterned lines, or allowed to grow in a random orientation and geometry on the two-dimensional surface. One-dimensional neurite alignment was achieved via microscale plasma-initiated patterning ( $\mu$ PIP) of laminin on lines with 2  $\mu$ m width [46, 47] (see also Materials and Methods).

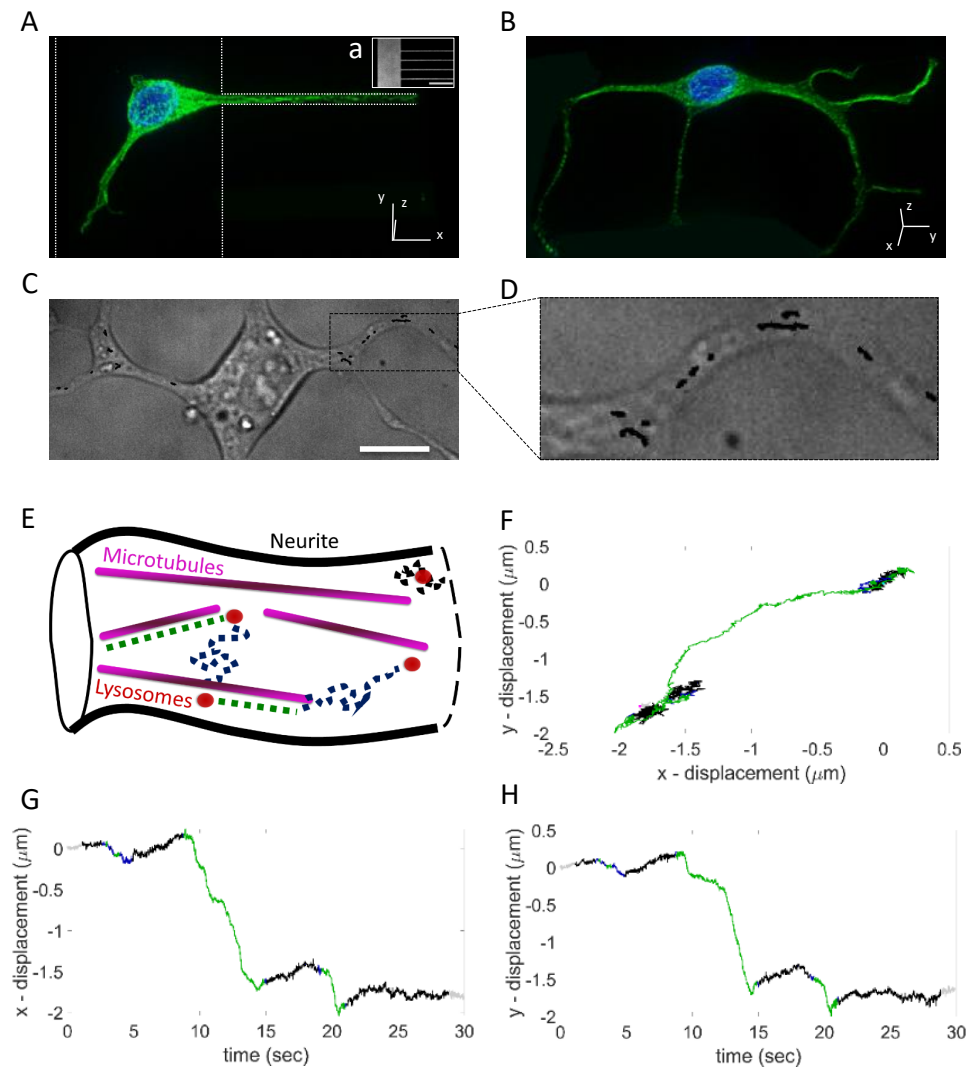


**Figure 4.1**

**Neurites configurations and time-resolved motility of lysosomes.** (A) Volume-view image of a differentiated PC12 cell with its neurite aligning along the  $2\mu\text{m}$ -wide patterned line. The white dashed line indicates the underlying protein pattern. Green color corresponds to alpha-tubulin and blue to the cell nucleus. Inset (a) shows the fluorescently-labeled patterned substrate, used to promote one-dimensional neurite guidance. Scale bar  $50\mu\text{m}$ . (B) Volume-view image of a differentiated PC12 cell with the neurites adopting random orientation on the flat substrate. Green color corresponds to alpha-tubulin and blue to the cell nucleus. (C) Bright-field image of a differentiated PC12 cell, overlaid with lysosomes trajectories (black lines). Scale bar  $10\mu\text{m}$ . (D) Close-up of the area indicated by the black square in (C). (E) Schematic of the three lysosome transport modes considered here, sub-diffusion (black dashed line), diffusion (blue dashed line) and super-diffusion, including active transport (green dashed line). (F) Displacement along the x- and y- axis of a lysosome trajectory, color-coded for the three transport modes: sub-diffusion (black), diffusion (blue) and super-diffusion (green). The motion mode of each trajectory data point was determined based on the  $\alpha$  exponent value, after fitting each lMSD with the power law ( $MSD(\tau) = A\tau^\alpha$ ) for lag times 0-555 msec (see also Materials and Methods). We considered  $\alpha < 0.9$  corresponds to sub-diffusive motion,  $0.9 \leq \alpha \leq 1.1$  corresponds to diffusive motion and  $\alpha > 1.1$  to super-diffusive motion. (G) and (H) Displacement along the x- and y- axis respectively, as a function of time, of the trajectory shown in (F).

Representative volume-view images of two differentiated PC12 cells and their neurites adopting the respective geometries are shown in Fig. 4.1.A and B. The pattern used to promote neurite guidance is demonstrated in the fluorescent image of inset Fig. 4.1.a, and indicated by the dashed white lines in Fig. 4.1.A. The thick side-stripe of the ladder-shape pattern allowed attachment of the cell body, and the dissecting  $2\mu\text{m}$ -wide lines guided the neurite outgrowth.

Trajectories of lysosomes inside neurites were monitored with fluorescence microscopy and their coordinates as a function of time were recorded. The number of cells, trajectories and data points per experimental condition are summarized in Table S.1. Fig. 4.1.C and D (close-up of the indicated area) show an example bright-field image of a differentiated cell, overlaid with recorded trajectories of lysosomes. To quantify the lysosomal dynamics, local mean-squared displacement (lMSD) analysis was implemented [46, 47, 58] (see also Materials and Methods). We considered a window of  $\sim 1\text{sec}$  before and after each data point to calculate the lMSD, which we subsequently fitted with the power law ( $MSD(\tau) = A\tau^\alpha$ ) for lag times  $\tau = 0 - 555\text{msec}$  [46]. Based on the resulting  $\alpha$  exponents, a time-resolved categorization of each trajectory data point was performed, into sub-diffusive ( $\alpha < 0.9$ ), diffusive ( $0.9 \leq \alpha \leq 1.1$ ) or super-diffusive ( $\alpha > 1.1$ ). The sketch in Fig. 4.1.E illustrates the three motion modes, and a lysosomal trajectory exhibiting all three modes is plotted in Fig. 4.1.F. Super-diffusive motion corresponds to large displacements in short time, with high directionality, as can be seen in Fig. 4.1.G and H. Diffusive and sub-diffusive motion result in smaller net displacements and a high degree of randomness.

Usually, diffusive or sub-diffusive states are intersected by rapid, super-

diffusive translocation, part of which potentially entails motor-mediated transport (for which  $\alpha \approx 2$ ) and other portions ( $\alpha > 1.1$ ) might be the result of thrust from the fibrillar network or from cytoplasmic flow. It is very common also that no active transport is observed within a trajectory, and the lysosome is undergoing only passive (sub-) diffusion. In fact, for all experimental conditions studied here, lysosomes spent a high fraction of their motion in the sub-diffusive mode as is evident by the probability distribution function of the  $\alpha$  exponent values show in Supplemental Figure S.2.

#### 4.2.2 Mean squared displacement and instantaneous velocity of lysosomes in cells with $G_4C_2$ repeats decrease notably inside aligned neurites.

To gain a comprehensive quantitative insight on the effect of the presence of the  $G_4C_2$  products on lysosomal motion, we first calculated the overall mean squared displacement (MSD) and the instantaneous velocity, averaged over all trajectories for each experimental condition.

As shown also previously [46], the MSD was higher for lysosomes inside aligned neurites in comparison to randomly oriented neurites for cells without the  $G_4C_2$  repeats (Fig. 4.2.A and B black, control). Concurrently, the instantaneous velocity was slightly increased for lysosomes inside aligned neurites (1D) of cells without the  $G_4C_2$  repeats, as shown in Fig. 4.2.C (black bars).

In the case where the cells carried the  $(G_4C_2)_{20}$  or  $(G_4C_2)_{39}$  repeats, lysosomes moving inside aligned neurites exhibited similar decrease in their MSD (Fig. 4.2.A) and average instantaneous velocity (Fig. 4.2.C), as compared to the control. Conversely, when the neurites were randomly oriented (2D), the lysosomal MSD exhibited a marginal decrease for cells transfected with  $(G_4C_2)_{20}$ , and was increased for cells with the  $(G_4C_2)_{39}$  repeats (Fig. 4.2.B). Consistent with the drop observed for aligned neurites, the instantaneous velocity of lysosomes inside randomly oriented neurites exhibited also a decrease, although smaller in comparison to the respective control.

Taken together, these results indicate that 1D neurite alignment not only gives rise to larger MSD but also slightly increased instantaneous velocity for lysosomes inside unperturbed cells, alongside with more distinct and consistent decrease of the respective values when the cells carry the  $(G_4C_2)_{20}$  or  $(G_4C_2)_{39}$  repeats. This consistency in the distinction of the repeats-associated perturbations in the MSD is not manifested in the case where lysosomal motion occurs in randomly oriented neurites. This is congruous with our previous results, where more efficient transport was observed for lysosomes inside aligned neurites, alongside with a more pronounced effect when a sucrose-induced perturbation was introduced inside the cellular environment [46].

## Effect of $G_4C_2$ Repeat Expansions on the Motion of Lysosomes

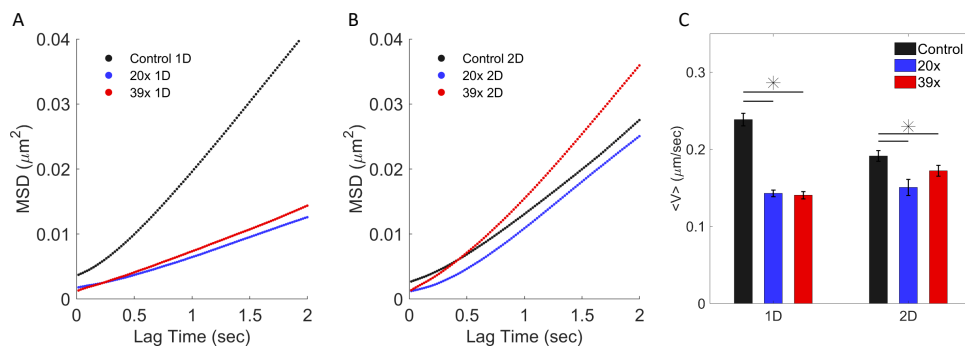


**Figure 4.2**

**Mean squared displacement (MSD) and average instantaneous velocity of lysosomal trajectories.** MSD of lysosomes inside (A) aligned (1D) and (B) randomly oriented (2D) neurites. (C) Average instantaneous velocity (the respective probability distributions of the instantaneous velocities for all conditions are shown in Supplemental Figure S.3). Values were calculated per trajectory and averaged over all lysosomal trajectories for each experimental condition (inside aligned (1D) or randomly oriented (2D) neurites, of differentiated PC12 cells without (control, black) or transfected with the  $G_4C_2$  repeat expansion (( $G_4C_2$ )<sub>20</sub>, blue, and ( $G_4C_2$ )<sub>39</sub>, red, respectively)). \* indicates significant difference ( $p \leq 0.05$ ), as determined using the Wilcoxon ranksum test. Error bars indicate the standard error of the mean.

### 4.2.3 Lysosomal maximum displacement and instantaneous velocity are decreased for all transport modes in the presence of the $G_4C_2$ repeats

The results presented in the previous subsection were considering whole-trajectory statistics. To gain a deeper insight into the lysosomal dynamics, we dissected every single trajectory into parts of each transport mode, namely super-diffusive, diffusive and sub-diffusive, as determined by the  $\alpha$  exponent value resulting from the lMSD analysis. Then, all the trajectory parts for each experimental condition and transport mode were collectively analyzed.

Figure 4.3 displays the maximum Euclidean displacement for super-diffusive (Fig. 4.3.A), diffusive (Fig. 4.3.B) and sub-diffusive (Fig. 4.3.C) motion modes for each experimental condition. The mean values and percentage decrease as compared to the respective controls are summarized in Table S.3. The maximum Euclidean displacement was the larger  $\Delta \mathbf{r}(t)$  calculated using eq.4.2 that was observed in the specific trajectory mode.

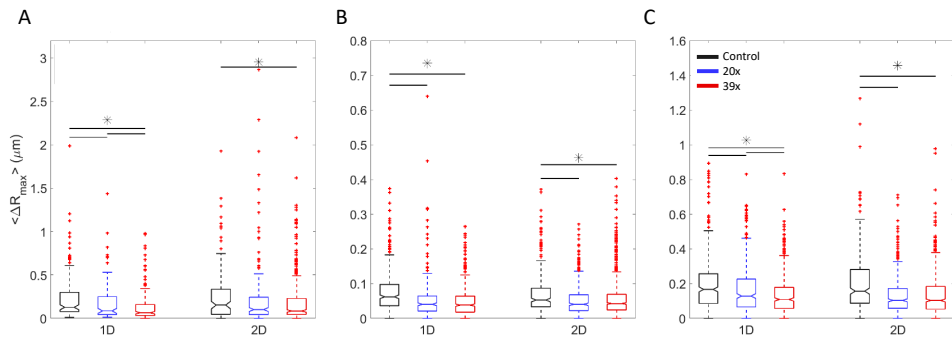
The results suggest that, in the control case, the mean value of the calculated maximum lysosomal displacement per transport mode exhibited negligible difference between the two neurite dimensionalities, whereas a consistent decrease is observed in the maximum Euclidean displacements for cells carrying the  $G_4C_2$  repeat expansions, for all lysosomal motion modes. Comparing the two neurite geometries, the decrease manifested in the super-diffusive and diffusive

lysosomal modes was stronger for aligned neurites, especially for the case of the  $(G_4C_2)_{39}$  repeats, while the opposite holds for the sub-diffusive modes. Interestingly, the percentage decrease in the aligned neurites case appeared to be increasing with higher repeats number (Table S.3).

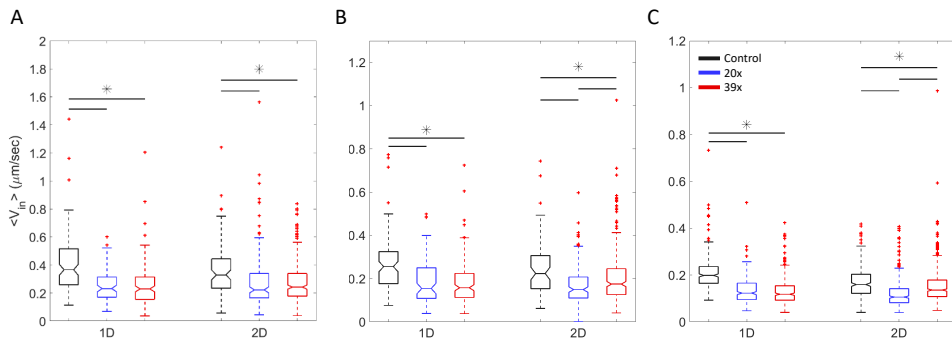
The Euclidean maximum displacement is a metric that can be affected by the duration of the trajectory mode as, for instance, longer trajectory parts might exhibit larger maximum displacements in comparison to shorter ones. Therefore, we next quantified the average instantaneous velocity per condition, whereby the displacement is normalized to the respective time step. The average instantaneous velocities for the different experimental conditions are presented in Figure 4.4 for super-diffusive (Fig. 4.4.A), diffusive (Fig. 4.4.B) and sub-diffusive (Fig. 4.4.C) motion modes. The mean values and percentage decrease as compared to the respective controls are summarized in Table S.4.

Conversely to the maximum displacement, neurite alignment appeared to slightly enhance lysosomal instantaneous velocity in the control condition (black, see also Table S.4). Moreover, a statistically significant decrease was observed for all transport modes, in both neurite dimensionalities in the presence of either repeats length, as compared to the respective values for cells without the  $G_4C_2$  repeats. Interestingly, when neurites were aligned the instantaneous velocity decrease per mode was similar for both HRE lengths, contrary to the case of randomly oriented neurites where the corresponding decrease was similar for super-diffusive modes, but differed for diffusive and sub-diffusive lysosomal transport modes, with the stronger decrease observed for sub-diffusive and diffusive motion states in the presence of  $(G_4C_2)_{20}$  repeats.

Collectively these results suggest that neurite dimensionality does not substantially affect the maximum Euclidean displacement of lysosomal trajectory modes in the control condition, but the average instantaneous velocity is slightly increased for all transport modes when the neurites are aligned, consistent with the overall instantaneous velocity shown in Fig. 4.2.C. However, when the disease-associated perturbation is introduced in the cells, a consistently larger decrease in the average instantaneous velocity is observed for the case where the neurites are aligned, especially in the super- and sub- diffusive motion modes.

**Figure 4.3**

**Maximum displacement of trajectory modes.** Boxplots of the maximum Euclidean displacement observed during (A) super-diffusive, (B) diffusive and (C) sub-diffusive trajectory modes, for all respective trajectory parts of lysosomes for each condition (aligned (1D) and randomly oriented (2D) neurites, of differentiated PC12 cells without (control, black) and with the  $G_4C_2$  repeat expansion ( $(G_4C_2)_{20}$ , blue and  $(G_4C_2)_{39}$ , red)). Boxplots indicate the median, whereas the mean values are displayed in Table S.3. \* indicates significant difference ( $p \leq 0.05$ ), as determined using the Wilcoxon ranksum test.

**Figure 4.4**

**Average instantaneous velocity of trajectory modes.** Boxplots of the average instantaneous velocity during (A) sub-diffusive, (B) diffusive and (C) super-diffusive trajectory modes, for all respective trajectory parts of lysosomes for each condition (aligned (1D) and randomly oriented (2D) neurites, of differentiated PC12 cells without (control, black) and with the  $G_4C_2$  repeat expansion ( $(G_4C_2)_{20}$ , blue and  $(G_4C_2)_{39}$ , red)). Boxplots indicate the median, whereas the mean values are displayed in Table S.4. \* indicates significant difference ( $p \leq 0.05$ ), as determined using the Wilcoxon ranksum test.

#### 4.2.4 Fitting parameters of transport modes MSD curves confirm the effect of the $G_4C_2$ repeat expansion.

Subsequently, we calculated the MSDs of the super-diffusive, diffusive and sub-diffusive parts of lysosomal trajectories. The plots are displayed in Fig. 4.5.A,B,C for aligned neurites (1D) and Fig. 4.5.D,E,F for randomly oriented neurites (2D). As shown previously, the MSD of lysosomes inside aligned (1D) neurites was higher than of those inside randomly oriented (2D) neurites, for all three motion modes considered, for cells that were not transfected with the repeats expansions (Fig. 4.5 control, black) [46].

To fit the super-diffusive MSD curves we implemented the model of Brownian motion with drift (eq. 4.6) [59]. For the diffusive MSDs, we used the Brownian motion model (eq. 4.7), and lastly the sub-diffusive MSD curves were fitted with a power law, commonly used to describe anomalous diffusion (eq. 4.8). The resulting fitting values of the drift velocity for the super-diffusive trajectory modes, diffusion coefficient of the diffusive modes, and  $\alpha$  exponent of the sub-diffusive modes, are summarized in Table S.5.

For the super-diffusive motion modes, the observed decrease in the MSD was similar for aligned (1D) neurites (Fig. 4.5.A), when the cells were transfected either with the  $(G_4C_2)_{20}$  (blue) or  $(G_4C_2)_{39}$  (red) repeats, and larger as compared to the respective drop for randomly oriented (2D) neurites (Fig. 4.5.D). The decrease is also reflected in the drift velocity of the super-diffusive trajectory parts ( $\sim 0.27\mu\text{m}/\text{sec}$  versus  $\sim 0.54\mu\text{m}/\text{sec}$  the control value for the aligned (1D) case and  $\sim 0.39\mu\text{m}/\text{sec}$  as compared to the control  $\sim 0.46\mu\text{m}/\text{sec}$  in the 2D case, summarized in Table S.5).

The MSD of the diffusive and sub-diffusive motion modes (Fig. 4.5.B and C), exhibited also similar decrease for lysosomes inside aligned neurites (1D) of cells transfected with the  $(G_4C_2)$  repeats, and consistently stronger in comparison to randomly oriented (2D) neurites. The diffusion coefficient of the diffusive lysosomal transport modes was reduced to almost half the respective control value for aligned neurites (1D), in the presence of both  $(G_4C_2)_{20}$  or  $(G_4C_2)_{39}$  repeats ( $\sim 0.0033\mu\text{m}^2/\text{sec}$  versus  $\sim 0.0065\mu\text{m}^2/\text{sec}$  the control value, summarized in Table S.5). Interestingly, for lysosomes inside randomly oriented neurites (2D) the MSD of diffusive and sub-diffusive motion modes was decreased more in the presence of the  $(G_4C_2)_{20}$  repeats (Fig. 4.5.E and F). Similarly, a decrease in the diffusion coefficient was only observed for the cells transfected with the  $(G_4C_2)_{20}$  repeats ( $\sim 0.0024\mu\text{m}^2/\text{sec}$ ), whereas it remained the same as the control value ( $\sim 0.0047\mu\text{m}^2/\text{sec}$ ) in the presence of  $(G_4C_2)_{39}$  repeats ( $\sim 0.0046\mu\text{m}^2/\text{sec}$ ).

The  $\alpha$  exponent of the sub-diffusive motion for cells transfected with  $(G_4C_2)_{20}$  or  $(G_4C_2)_{39}$ , was decreased as compared to the control, more prominently when the neurites adopted a random geometry, contrary to the aligned case where it was unaffected for the  $(G_4C_2)_{20}$  repeats and slightly decreased

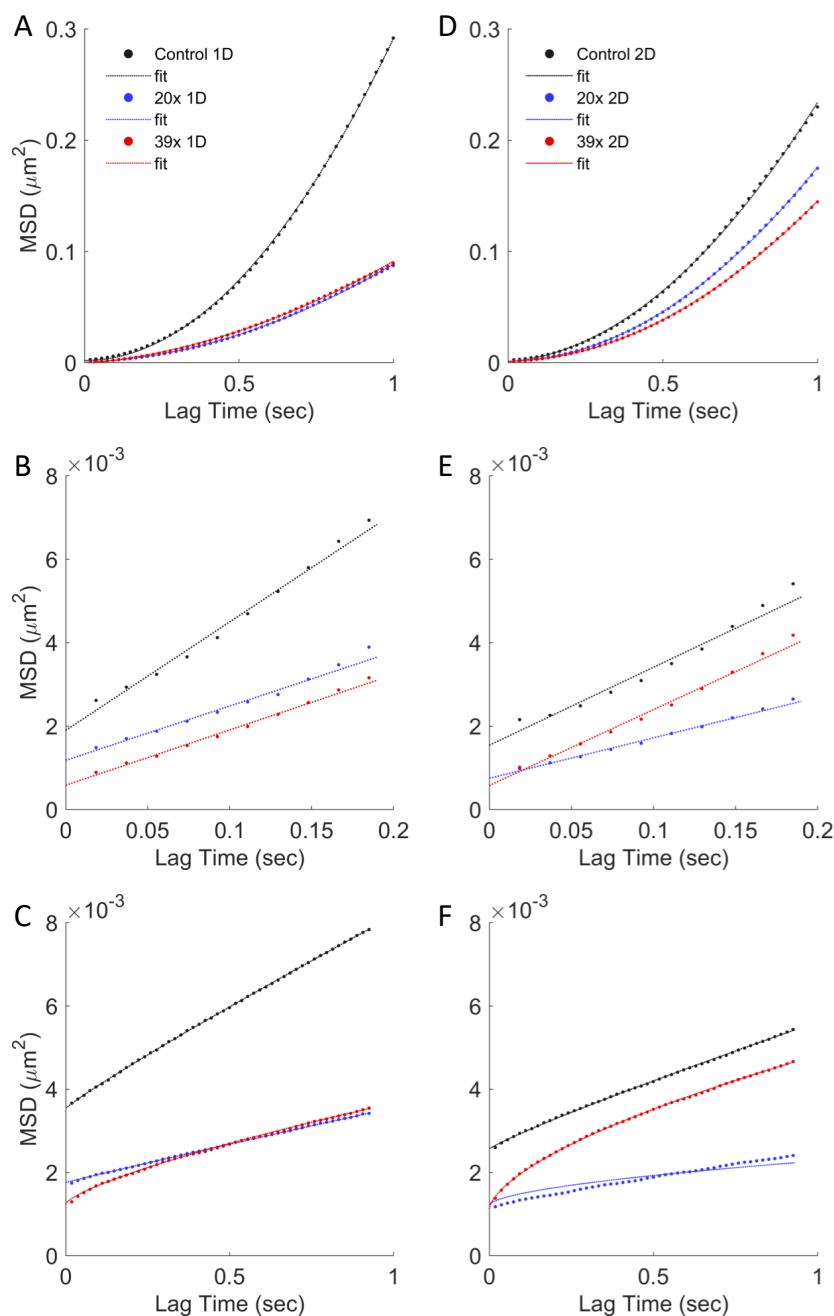


**Figure 4.5**

**MSD plots of motion modes.** MSD plots and respective fits of (A), (D) super-diffusive, (B), (E) diffusive and (C), (F) sub-diffusive trajectory modes for aligned (1D, A-C) and randomly oriented (2D, D-F) neurites, respectively. The MSDs were calculated by averaging over all the respective trajectory parts of lysosomes for each condition: without (control, black) or transfected with the  $G_4C_2$  repeat expansion ( $(G_4C_2)_{20}$ , blue and  $(G_4C_2)_{39}$ , red, respectively). The MSD curves were fitted using eq. 4.6-4.8 and the resulting values of the fitting parameters are summarized in Table S.5.

for the  $(G_4C_2)_{39}$  repeats (Table S.5).

Taken all together, these results suggest that upon introducing the disease-associated perturbation, the decline in the MSD for all transport modes of lysosomes inside aligned neurites is similar for both repeats expansions and more distinct in comparison to randomly oriented neurites, especially for super- and diffusive motion states and their respective drift velocities and diffusion coefficients. However, for the sub-diffusive motion states, the  $\alpha$  exponent of lysosomes inside randomly oriented (2D) neurites is more sharply decreased, perhaps suggesting a more pronounced crowding effect resulting from the presence of the  $(G_4C_2)$  repeats in this geometry.

#### 4.2.5 The ratio of anterograde/retrograde/neutral super-diffusive lysosomal trajectories varies for the two neurite geometries but exhibits similar instantaneous velocity differences.

Lastly, we investigated whether the presence of the  $G_4C_2$  repeat expansion in the cells had a different effect on lysosomal motion towards (retrograde) or away from (anterograde) the cell body. To this end, we categorized accordingly all trajectories that included a portion of super-diffusive motion, based on their net displacement (end point versus start point). In occasions where the net displacement was zero or perpendicular to the axis pointing towards or away from the cell body, the trajectory was labeled as neutral.

The proportion of each type of net trajectory directionality for every experimental condition is summarized in Fig. 4.6.A. In the control case for randomly oriented neurites the portion of anterograde/retrograde/neutral trajectories appears to be equally distributed, whereas in the aligned scenario lysosomes exhibit less neutral net displacement and more anterograde motion. Moreover, it appears that inside aligned neurites, more trajectories exhibited a neutral net displacement and less lysosomes moved away from the cell body when the cells carried the repeat expansion, as compared to the control case. Surprisingly, the exact opposite was observed for lysosomes inside neurites of a random geometry: less trajectories appear to have a neutral net displacement and more lysosomes moved away from the cell body when the cells carried the repeat expansion.

In addition, the mean instantaneous velocities of both super-diffusive ( $\alpha > 1.1$ , Fig. 4.6.B) and (sub-)diffusive ( $\alpha \leq 1.1$ , Fig. 4.6.C) data points of these trajectories exhibited similar decrease regardless the direction of motion (anterograde or retrograde) or the size of the repeats, for lysosomes inside aligned neurites. The same trend was maintained for lysosomes inside randomly oriented neurites, but with a smaller decrease compared to the aligned scenario, and almost negligible for data points with  $\alpha \leq 1.1$ . Interestingly, for this subset of trajectories, the average instantaneous velocity was similar for both geometries in the control case ( $\sim 0.4\mu\text{m}/\text{sec}$  for  $\alpha > 1.1$  and  $\sim 0.2\mu\text{m}/\text{sec}$  for

$\alpha \leq 1.1$ ).

To summarize, these results indicate that the ratio of anterograde/retrograde/neutral trajectories varies between the two neurite geometries and changes differently in the presence of the  $(G_4C_2)$  repeats. On the contrary, the decrease observed in the instantaneous velocity when the cells carry the repeats, is similar for anterograde/retrograde motion in each respective neurite geometry, with the exception for data points with  $\alpha \leq 1.1$  inside randomly oriented neurites.

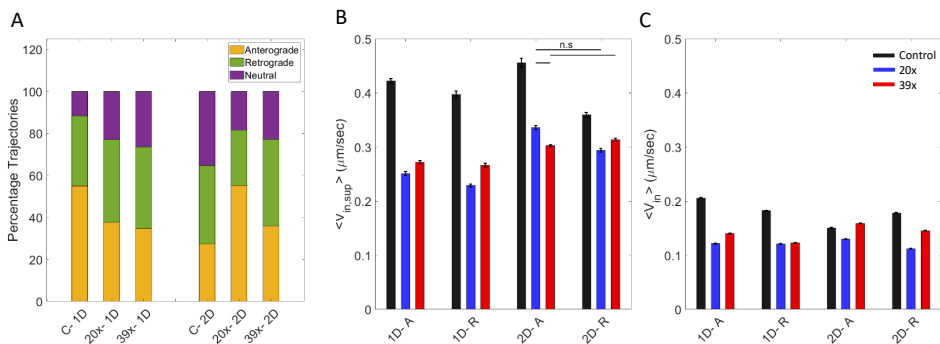


**Figure 4.6**

**Statistics on anterograde and retrograde trajectories entailing super-diffusive motion.** (A) Percentage of lysosomal trajectories exhibiting super-diffusive motion, distinguished according to their net displacement either towards (retrograde) or away from (anterograde) the cell body for each condition: inside aligned (1D) and randomly oriented (2D) neurites, of differentiated PC12 cells without (control) and with the  $G_4C_2$  repeat expansion ( $(G_4C_2)_{20}$  and  $(G_4C_2)_{39}$ , respectively). In all cases, trajectories categorized as neutral didn't exhibit a net displacement towards either direction. (B) Average instantaneous velocity of data points with  $\alpha > 1.1$  and (C) average instantaneous velocity of data points with  $\alpha \leq 1.1$ , from lysosomal trajectories with super-diffusive motion, exhibiting anterograde (A) or retrograde (R) net displacement inside aligned (1D) and randomly oriented (2D) neurites of differentiated PC12 cells. The mean values of the distributions were compared using the Wilcoxon ranksum test and they exhibited significant difference ( $p \leq 0.05$ ), unless indicated otherwise. The values of the average instantaneous velocities are summarized in Table S.6.

### 4.3 Discussion

The protein encoded by the *c9orf72* locus is implicated with the autophagy-lysosome pathway [29, 34, 60–69], and lysosome homeostasis [60, 70], while recent reports suggest the associated  $G_4C_2$  repeat expansion mutation causes deficient axonal transport of mitochondria [40] and lysosomes [41] in neurons. Here, we set our focus on quantifying lysosomal motility inside neurites of differentiated PC12 cells without or transfected with plasmids containing either  $(G_4C_2)_{20}$  or  $(G_4C_2)_{39}$ . For both repeat lengths used in this study, patient cases have been identified and experimental models have been reported to recapitulate pathological hallmarks [10–15].

Cell shape, greatly affected by the ECM, can influence intracellular trafficking among other processes [71–73]. In the experiments presented here, in addition to quantitatively investigating the effect of the  $G_4C_2$  repeat expansion on lysosomal trafficking inside neurites, we were in parallel looking into how the neurite dimensionality interferes with the motion. Thereby, using our previously established experimental setup [46], the neurites were either guided to grow along chemically-patterned lines, or allowed to adopt a random orientation on the two-dimensional surface, thus enabling observation of lysosomal motility inside neurites of two distinct geometries. Braun et al. have reported that neurite orientation influences the severity of mechanically-induced tau pathology, and found that neurons with neurites aligned parallel to stretch orientation showed significantly greater tau mislocalization than those aligned perpendicular to stretch or with no alignment when exposed to high-strain-rate strains, in an *in vitro* tauopathy model of traumatic brain injury (TBI) [74]. We have previously found that neurite alignment gives rise to faster lysosomal motility, and that a sucrose-induced perturbation in the intracellular environment hampers lysosomal motion variably for the aligned or randomly oriented neurites [46]. The current findings support the notion that neurite alignment results in more efficient transport, via yielding slightly increased lysosomal instantaneous velocity in addition to larger MSD for all transport modes in the control condition. Moreover, when the cells were transfected with the  $(G_4C_2)_{20}$  or  $(G_4C_2)_{39}$  repeats, the aligned neurite geometry associated with greater decrease in both the overall lysosomal instantaneous velocity and MSD, as compared to neurites that were randomly oriented, also consistently suggesting a stronger effect in response to the perturbation in the cellular environment when the neurites were aligned.

Our results suggested that lysosomal motility was largely sub-diffusive regardless the neurite geometry or the presence of the HRE. Nonetheless, after analyzing separately each lysosomal motion state, a consistent decrease in both the average instantaneous velocity and MSD of all motion modes was evident upon introducing the HRE perturbation. The drop was consistently larger when the neurites were aligned, particularly in the average instantaneous velocity

of the super- and sub- diffusive motion modes, and the MSD of all transport modes.

Arginine-rich DPR proteins such as the poly-GR have been known for their high expression, as compared to other DPR proteins, and their correlation with pathological phenotypes [26, 53, 54, 56, 57]. Fumagalli et al. recently offered more insights on the connection between this DPR proteins species and axonal transport, and suggested a model where arginine-rich DPR proteins bind microtubules and concentrate in microtubule-associated foci, thereby disrupting the binding of motor proteins and subsequently efficient intracellular trafficking [41]. Notably, the drift velocity and diffusion coefficient values we obtained from the MSD for lysosomes inside cells transfected with (G<sub>4</sub>C<sub>2</sub>)<sub>20</sub> and (G<sub>4</sub>C<sub>2</sub>)<sub>39</sub>, are similar in the case where the neurites were aligned. This suggests that (G<sub>4</sub>C<sub>2</sub>)<sub>20</sub> producing arginine-rich DPR proteins, affects super-diffusive and diffusive lysosomal motion equally as the double repeats length (G<sub>4</sub>C<sub>2</sub>)<sub>39</sub> producing alanine-rich DPR proteins for this neurite geometry. However, for the randomly oriented neurites, the diffusion coefficient remained unchanged in the presence of the (G<sub>4</sub>C<sub>2</sub>)<sub>39</sub> repeats whereas the super-diffusive drift velocity slightly decreased with increasing repeats length. These findings do not consistently support the hypothesis of repeats length-dependent toxicity or disease onset [13, 75–80], but this could be attributed to the similar size of the HRE used in the present experiments. Additionally, a potential crowding effect was only evident via the decrease in the sub-diffusive  $\alpha$  exponent in the presence of the (G<sub>4</sub>C<sub>2</sub>)<sub>39</sub> repeats for lysosomes inside both neurites geometries.

Moreover, Abo-Rady et al. also reported decreased lysosomal displacement inside axons of patient-derived motor neurons, but no significant alterations in the directionality of lysosomal trafficking [40]. Our maximum Euclidean displacement and MSD results are in agreement with those findings. Interestingly, we observed lysosomal motility directionality alterations in cells transfected with the repeats, which varied with the neurite geometry, accompanied by relatively consistent decrease in the instantaneous velocity for both repeat sizes and geometries.

In summary, the results presented here support the hypothesis that the HRE affects organelle trafficking, and reveal an interplay with the geometry of the neurite: although neurite alignment results in faster lysosomal motility with larger MSD, when the HRE are present, the homeostasis disruption is more evident as compared with the randomly oriented neurites. Our work presents a preliminary approach and the experimental system and analysis used provide a phenomenological description and entails a number of limitations. First of all, we only quantified the transfected HRE RNA levels via FISH. In future work, protein levels should be analyzed, alongside with correlations with the RNA levels, and protein degradation rates, to investigate if the two residue repeat peptides contribute to, or are the underlying cause of, the observed changes, and gain a deeper insight into the respective associated mechanisms.

Secondly, here we used plasmids carrying  $(G_4C_2)_{20}$  or  $(G_4C_2)_{39}$ , preceded by a start codon aligned such as to result in the production of  $(GR)_{20}$  or  $(GA)_{39}$ , respectively. The differences in both repeat number and translation frame poses a difficulty in the interpretation of the results and direct correlation with the two HREs. Future work should not only include an additional control group with  $(G_4C_2)_{2-19}$ , as observed in healthy individuals, but also explore same and longer repeats numbers coding for same dipeptide repeat proteins, to distinguish the associations between organelle motility with repeats length and protein products. Lastly, the neurite geometries need to be further explored and characterized, to elucidate potential interplay with the polarity of the microtubule network, neurite size, diameter and branching. We hope this work will set the basis for further experimental exploration to obtain deeper biophysical, mechanistic, and physiological insights on the effect of the  $G_4C_2$  repeat expansion on axonal trafficking.

## 4.4 Materials and Methods

### 4.4.1 Laminin $\mu$ PIP

Plasma-initiated patterning of the substrate was performed as described previously [46]. Briefly, a mold was fabricated with a Nanoscribe Photonic professional GT 3D laser printer (Nanoscribe, Germany), with two-photon polymerization (2PP) of IP-S photoresist [81].

Poly dimethyl-siloxane (PDMS, Sylgard 184, Dow Corning, USA) was prepared by mixing the cross-linking agent with the elastomer base at a ratio of 1:10. The mixture was pipetted on the silicon mold and allowed to cross-link for 1 hour at 120°C. Subsequently, the hardened PDMS bearing the structure was peeled from the wafer.

The PDMS mask was placed on an ibidi dish (ibidi GMBH,  $\mu$ -Dish, 35 mm high, polymer coverslip bottom), with the structure-bearing side adherent to the bottom of the dish and was exposed to air plasma for 6 min 20 sec at 100 Watts (Diener Electronic Femto Plasma system).

Subsequently, the PDMS mask was removed and the substrate was flooded with 0.1% Pluronic F127 (Sigma-Aldrich) diluted in Phosphate Buffer Saline (PBS) for 45 minutes at room temperature. The dish was then washed 3 times with PBS and once with RPMI (Gibco<sup>TM</sup>) and subsequently incubated with 25 $\mu$ g/ml Laminin (Sigma-Aldrich) diluted in RPMI, for 1 hour at 37°C. Prior to seeding cells, the substrate was washed 3 times with RPMI.

### 4.4.2 Cell Culture

PC12 cells (CH3 BioSystems) were cultured in dishes coated with rat-tail Collagen (CH3 BioSystems), in RPMI-1640 with Glutamax (Gibco<sup>TM</sup>), supplemented with 10% heat-inactivated Horse Serum (HS) (Sigma-Aldrich), 5% Fetal Calf Serum Heat Inactivated (FCS HI, Thermo Scientific) and 200 $\mu$ g/mL penicillin/streptomycin (PS). Media were refreshed three times per week, and the cells were split once per week at ratio 1:3-1:6. The cells were kept at 37°C and 5% CO<sub>2</sub> in humidified atmosphere.

To induce differentiation, PC12 cells were seeded in ibidi uncoated dishes (ibidi GMBH,  $\mu$ -Dish, 35 mm high) coated with Laminin (Sigma-Aldrich). Cells were seeded at a density of 30.000 cells/cm<sup>2</sup> in full media and after they had adhered, they were washed once with PBS and then the media were replaced with differentiation media consisting of Opti-MEM<sup>TM</sup> Reduced Serum Medium (Gibco<sup>TM</sup>) supplemented with 0.5% Fetal Bovine Serum (Gibco<sup>TM</sup>) and Nerve Growth Factor (NGF-2.5S Sigma-Aldrich) at final concentration of 100ng/ml. The differentiation media were refreshed three times per week.

Prior to imaging, the cells were incubated with 50-150nM Lyotracker (Invitrogen<sup>TM</sup>) in RPMI for 30minutes.

Two plasmids, containing either 20 or 39 times the  $G_4C_2$  sequence were created (GenScript) and amplified using NEB@Stable Competent *E.coli* bacteria (High Efficiency, New England BioLabs Inc.), according to the protocol for cloning DNA containing repeat elements (C3040, New England BioLabs Inc.). In both plasmids, the  $G_4C_2$  repeat expansion was preceded by a start codon (ATG) and the reading frames were aligned such that the  $(G_4C_2)_{20}$  resulted in  $(GR)_{20}$  and the  $(G_4C_2)_{39}$  resulted in  $(GA)_{39}$  DPR proteins.

For transfection,  $\sim 5.7 \times 10^5$  PC12 cells were seeded in each well of a Collagen-coated 6-well plate, and the next day they were transfected, using Lipofectamine LTX PLUS (Thermo-Fisher Scientific), with  $2\mu\text{g}$  of the  $(G_4C_2)_{20}$  or  $(G_4C_2)_{39}$  expression constructs per well. After a three-day incubation, Geneticin (G418, Thermo-Fisher Scientific) was added for selection of the transfected cells. After several days of selection, the cells were sparsely re-seeded on Collagen-coated 10-cm dishes to create single-cell clones, which were subsequently transferred to a Collagen-coated 96-well plate.

Successfully transfected clones were verified using single-molecule Fluorescent *in situ* Hybridization (smFISH). Briefly, the cells were fixed for 15 minutes with 4% PFA at room temperature and permeabilized overnight in 70% EtOH. Next, the custom-designed smFISH probes (LGC Biosearch Technologies, targeting 5' GGCCCC GGCCCC GGCCCC GGCCCC 3') were added at a concentration of 1:100 in hybridization buffer (100 mg/mL dextran sulfate, 25% formamide, 2X SSC, 1 mg/mL *E.coli* tRNA, 1 mM vanadyl ribonucleoside complex, 0.25 mg/mL BSA) and allowed to incubate for 16 hours at  $30^\circ\text{C}$ . Thereafter, the cells were washed twice with washing buffer (25% formamide, 2X SSC) containing DAPI (1 mg/mL, Sigma Aldrich), for 30 minutes at  $30^\circ\text{C}$ . All solutions were prepared using RNase-free water. Lastly, the cells were mounted with Prolong Gold (Thermo-Fisher Scientific) and imaged two days later.

For immunofluorescence, differentiated PC12 cells were fixed with 4% PFA for 15 minutes at room temperature, permeabilized with 0.1% TritonX for 10 minutes and blocked with 2% BSA in PBS for 60 minutes. Subsequently the cells were incubated with the  $\alpha$ -tubulin antibody (Alexa Fluor®488 anti-alpha Tubulin antibody, abcam) 1:150 in 0.1% BSA in PBS at  $4^\circ\text{C}$  for 18 hours. Lastly, the cells were incubated for 30 minutes at room temperature with Hoechst (Invitrogen) diluted to  $1\mu\text{g}/\text{ml}$  in 1% BSA in PBS and stored in PBS at  $4^\circ\text{C}$  until imaging.

#### 4.4.3 Optical Microscopy

Optical microscopy images were acquired with a Nikon Ti Eclipse inverted microscope (NIKON corporation, Japan) equipped with a Yokogawa CSU-X1 spinning disc unit (10,000rpm, Andor Technology Ltd., United Kingdom). The samples were imaged with a 100x objective (Nikon CFI Plan Apo Lamda, NA

1.45). Excitation at 405nm, 488nm and 647nm was achieved via an Agilent MLC400 monolithic laser combiner (Agilent Technologies, Netherlands). The excitation light was filtered by a custom-made Semrock quad-band dichroic mirror for excitation wavelengths 400-410, 486-491, 460-570, and 633-647nm. The emitted light was filtered using a Semrock quad-band fluorescence filter (TR-F440-521-607-700), which has specific transmission bands at  $440\pm 40\text{nm}$ ,  $521\pm 21\text{nm}$ ,  $607\pm 34\text{nm}$  and  $700\pm 45\text{nm}$  and by Semrock Brightline single band fluorescence filters at  $447\pm 60\text{nm}$  (TR-F447-060) and  $525\pm 60\text{nm}$  (TR-F525-030). Images were captured with an Andor iXon Ultra 897 High-speed EM-CCD camera. Image acquisition was automated using NisElements software (LIM, Czech Republic). Time-lapse images were acquired every 18 ms, for up to 30 seconds. During data acquisition, the cells were kept in a humidified atmosphere at 37°C and supplied with 5% CO<sub>2</sub> via the use of a Tokai Hit stage incubator.

#### 4.4.4 Data Analysis

FISH signal quantification was performed with FIJI [82]. The integrated fluorescent intensity per cell nucleus was measured, after maximum intensity projection of the volume-view acquired images, and the values were averaged for a number of cells,  $N$ , per condition.

For each experimental condition, at least 3 technical replicates were used. The number of cells, trajectories and data points per experimental condition are summarized in Table S.1. The control condition data are the same as those presented in [46]. Fluorescently labelled lysosomes trajectories were tracked using the FIJI plugin, TrackMate [83], which returned the  $x$ - and  $y$ -coordinates of the center of the lysosomes, with a sub-pixel localization.

Further processing was performed using home-made Matlab algorithms. The  $x$ - and  $y$ - coordinates as a function of time for each trajectory were represented by a series of vectors at each time point  $t$ :

$$\mathbf{r}(t) = x(t) + y(t) \quad (4.1)$$

and the displacement  $\Delta\mathbf{r}$  at time  $t$  was calculated as follows:

$$\Delta\mathbf{r}(t) = \mathbf{r}(t + \Delta t) - \mathbf{r}(t) \quad (4.2)$$

where  $\Delta t$  is the inverse frame rate.

The instantaneous velocity  $v(t)$  was calculated using:

$$v(t) = \frac{|\Delta\mathbf{r}(t)|}{\Delta t} \quad (4.3)$$

for  $\Delta t = 314.5\text{msec}$  (17 frames).

The Mean Squared Displacement (MSD) for lag time  $\tau = k\Delta t$  was calculated according to:

$$MSD(\tau) = \langle \Delta \mathbf{r}^2(\tau) \rangle = \frac{1}{N-k} \sum_{i=1}^{N-k} (\mathbf{r}(t_i + \tau) - \mathbf{r}(t_i))^2 \quad (4.4)$$

where  $N$  the number of data points in the trajectory and  $k = 1, 2, \dots, N - 1$ . The average MSD per condition is the average of the squared displacements of all lysosome trajectories for each lag time  $\tau$ .

The local Mean Squared Displacement (lMSD) was calculated for each trajectory as described previously [46]. Briefly, the MSD was calculated for each data point of the entire trajectory using a rolling window of 2.22 seconds ( $N=120$ , in eq. 4.4) and fitted for the interval 0-555ms ( $k=30$  in eq. 4.4) with a power law:

$$MSD(\tau) = A\tau^\alpha \quad (4.5)$$

The alpha exponent as a function of time was subsequently used to partition the transport states as sub-diffusive for  $\alpha < 0.9$ , diffusive for  $0.9 \leq \alpha \leq 1.1$ , or super-diffusive for  $\alpha > 1.1$ .

In order to characterize more closely each type of motion, we analyzed collectively the respective trajectory parts, for each experimental condition (lysosomes inside neurites that were aligned or randomly oriented, of differentiated PC12 cells without the repeat expansion (control) or with 20x and 39x the  $G_4C_2$  repeats). The respective statistics are summarized in Table S.2.

The average MSD curve for each motion mode was calculated again according to eq. 4.4.

The super-diffusive trajectory modes MSD was fitted using the model of Brownian motion with drift [59].

$$MSD(\tau) = 2dD_{eff}\tau + V^2\tau^2 + 2d\sigma^2 \quad (4.6)$$

where  $V_{drift}$ , the constant drift parameter models the velocity of the molecular motors. The MSD curve was fitted for lag times 1 to 55 ( $\tau$  between 0.0185 and 1 sec).

The diffusive trajectory modes MSD was fitted using the equation describing Brownian motion

$$MSD(\tau) = 2dD\tau + 2d\sigma^2 \quad (4.7)$$

thus extracting the experimental value of the diffusion coefficient  $D$ . The MSD curve was fitted for lag times 1 to 10 ( $\tau$  between 18.5 and 185 ms).

The sub-diffusive trajectory modes MSD was fitted with the power law describing anomalous diffusion

$$MSD(\tau) = A\tau^\alpha + 2d\sigma^2 \quad (4.8)$$

thereby obtaining the value of the anomalous  $\alpha$  exponent ( $A$  is a constant). The MSD curve was fitted for all lag times ( $\tau$  up to 30 sec).

In equations 4.6, 4.7 and 4.8  $\sigma$  is the localization precision,  $\tau$  the lag time and the parameter  $d$  refers to the dimensionality.  $d$  was set equal to 1 for the fit of the MSD along the x- or y- axis, and equal to 2 for the fit of the 2D- MSD curve.

## 4.5 Appendix

	# Cells	# Trajectories	# Data Points
1D			
Control	19	167	188542
20x	15	194	265191
39x	21	167	247946
2D			
Control	16	178	230196
20x	14	219	304326
39x	13	204	298387

**Table S.1**

Number of cells imaged, number of total lysosomal trajectories tracked and number of total data points per experimental condition (differentiated PC12 cells without (control) or with the  $G_4C_2$  repeats (20x and 39x), with their neurites aligned or randomly oriented, denoted by 1D and 2D, respectively).

	Super-diffusive		Diffusive		Sub-diffusive	
	# Modes	# Data Points	# Modes	# Data Points	# Modes	# Data Points
1D						
Control	135	8254	334	5484	352	154732
20x	117	8379	275	4649	340	228792
39x	204	11833	497	8751	446	207195
2D						
Control	117	8029	257	4504	307	196326
20x	210	13378	451	7889	451	256722
39x	185	27366	912	15205	681	231289

**Table S.2**

Number of lysosomal trajectories parts (modes) and number of total data points per mode, for each experimental condition (differentiated PC12 cells without (control) or with the  $G_4C_2$  repeats (20x and 39x), with their neurites aligned or randomly oriented, denoted by 1D and 2D, respectively).

	Super-diffusive		Diffusive		Sub-diffusive	
1D						
Control	0.251 ± 0.025		0.078 ± 0.003		0.200 ± 0.008	
20x	0.182 ± 0.021	27%	0.055 ± 0.004	29%	0.170 ± 0.008	15%
39x	0.140 ± 0.013	44%	0.049 ± 0.002	37%	0.139 ± 0.005	30%
2D						
Control	0.265 ± 0.030		0.074 ± 0.004		0.210 ± 0.010	
20x	0.223 ± 0.025	16%	0.054 ± 0.002	27%	0.130 ± 0.005	38%
39x	0.203 ± 0.018	23%	0.056 ± 0.002	24%	0.136 ± 0.005	35%

**Table S.3**

Mean values of the maximum Euclidean displacement observed during super-diffusive, diffusive and sub-diffusive trajectory modes (in  $\mu\text{m}$ ). The values were averaged over all the respective trajectory parts of lysosomes for each condition (inside aligned (1D) and randomly oriented (2D) neurites, of differentiated PC12 cells without (control) and with the G<sub>4</sub>C<sub>2</sub> repeat expansion ((G<sub>4</sub>C<sub>2</sub>)<sub>20</sub> or (G<sub>4</sub>C<sub>2</sub>)<sub>39</sub>). Errors were calculated using the standard error of the mean. The distributions of the values for each condition are displayed in Fig. 4.3. The percentages next to the 20x and 39x values indicate the decrease as compared to the respective control.

	Super-diffusive		Diffusive		Sub-diffusive	
1D						
Control	0.395 ± 0.019		0.271 ± 0.007		0.208 ± 0.004	
20x	0.249 ± 0.010	37%	0.186 ± 0.006	31%	0.134 ± 0.003	36%
39x	0.250 ± 0.010	37%	0.179 ± 0.004	34%	0.132 ± 0.003	36%
2D						
Control	0.362 ± 0.018		0.253 ± 0.008		0.170 ± 0.004	
20x	0.282 ± 0.014	22%	0.173 ± 0.004	32%	0.122 ± 0.003	28%
39x	0.276 ± 0.007	24%	0.207 ± 0.004	18%	0.153 ± 0.003	10%

**Table S.4**

Mean values of the instantaneous velocity during super-diffusive, diffusive and sub-diffusive trajectory modes (in  $\mu\text{m}/\text{sec}$ ). Values were averaged over all the respective trajectory parts of lysosomes for each condition (inside aligned (1D) and randomly oriented (2D) neurites, of differentiated PC12 cells without (control) and with the G<sub>4</sub>C<sub>2</sub> repeat expansion ((G<sub>4</sub>C<sub>2</sub>)<sub>20</sub> or (G<sub>4</sub>C<sub>2</sub>)<sub>39</sub>). Errors were calculated using the standard error of the mean. The distributions of the values for each condition are displayed in Fig. 4.4. The percentages next to the 20x and 39x values indicate the decrease as compared to the respective control.

	Super-diffusive		Diffusive	Sub-diffusive
	$V_{drift}$ ( $\mu\text{m}/\text{sec}$ )	$D_{eff}$ ( $\mu\text{m}^2/\text{sec}$ )	D ( $\mu\text{m}^2/\text{sec}$ )	$\alpha$ - exponent
1D				
Control	$0.538 \pm 0.008$	$6E - 7 \pm 0.002$	$0.0065 \pm 0.0013$	$0.92 \pm 0.01$
20x	$0.278 \pm 0.007$	$0.003 \pm 0.001$	$0.0033 \pm 0.0006$	$0.97 \pm 0.04$
39x	$0.258 \pm 0.009$	$0.006 \pm 0.001$	$0.0033 \pm 0.0005$	$0.74 \pm 0.05$
2D				
Control	$0.460 \pm 0.010$	$0.005 \pm 0.002$	$0.0047 \pm 0.0015$	$0.90 \pm 0.03$
20x	$0.413 \pm 0.004$	$0.001 \pm 0.001$	$0.0024 \pm 0.0003$	$0.57 \pm 0.64$
39x	$0.373 \pm 0.003$	$0.001 \pm 0.001$	$0.0046 \pm 0.0007$	$0.62 \pm 0.02$
	$\sigma$ ( $\mu\text{m}$ )		$\sigma$ ( $\mu\text{m}$ )	$\sigma$ ( $\mu\text{m}$ )
1D				
Control		$0.022 \pm 0.022$	$0.022 \pm 0.012$	$0.030 \pm 0.003$
20x		$0.008 \pm 0.015$	$0.017 \pm 0.008$	$0.021 \pm 0.003$
39x		$0.000 \pm 0.014$	$0.012 \pm 0.007$	$0.018 \pm 0.004$
2D				
Control		$0.015 \pm 0.023$	$0.020 \pm 0.012$	$0.025 \pm 0.003$
20x		$0.019 \pm 0.014$	$0.014 \pm 0.006$	$0.017 \pm 0.012$
39x		$0.018 \pm 0.011$	$0.012 \pm 0.009$	$0.017 \pm 0.004$

**Table S.5**

Motion parameters resulting from fitting the super-diffusive, diffusive and sub-diffusive trajectory parts MSD curves (demonstrated in Fig. 4.5), using eq. 4.6, 4.7 and 4.8, respectively.

	$V_{in,sup}$ ( $\mu\text{m}/\text{sec}$ )		$V_{in}$ ( $\mu\text{m}/\text{sec}$ )	
	Anterograde	Retrograde	Anterograde	Retrograde
1D				
Control	$0.422 \pm 0.004$	$0.398 \pm 0.006$	$0.206 \pm 0.001$	$0.182 \pm 0.001$
20x	$0.251 \pm 0.003$	$0.229 \pm 0.003$	$0.122 \pm 0.001$	$0.121 \pm 0.001$
39x	$0.272 \pm 0.003$	$0.267 \pm 0.003$	$0.140 \pm 0.001$	$0.123 \pm 0.001$
2D				
Control	$0.456 \pm 0.008$	$0.360 \pm 0.004$	$0.150 \pm 0.001$	$0.178 \pm 0.001$
20x	$0.336 \pm 0.003$	$0.294 \pm 0.004$	$0.130 \pm 0.001$	$0.112 \pm 0.001$
39x	$0.303 \pm 0.002$	$0.314 \pm 0.002$	$0.159 \pm 0.001$	$0.146 \pm 0.001$

**Table S.6**

Average instantaneous velocity during anterograde or retrograde motion of lysosomal trajectories. Values were calculated separately for data points with  $\alpha > 1.1$  (indicated as "sup") or  $\alpha \leq 1.1$ , from trajectories with super-diffusive motion, exhibiting anterograde or retrograde net displacement inside aligned (1D) and randomly oriented (2D) neurites of differentiated PC12 cells without (control) and with the  $G_4C_2$  repeat expansion ( $(G_4C_2)_{20}$  and  $(G_4C_2)_{39}$ , respectively). Errors represent the standard error of the mean. The respective distributions are shown in Fig. 4.6.B and C.

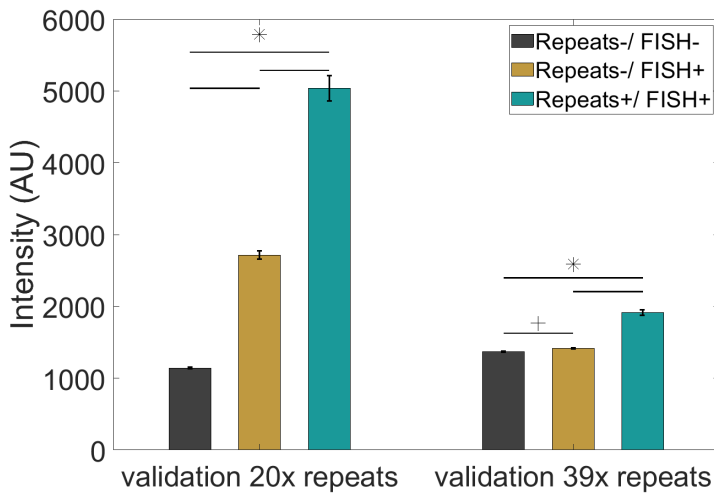


**Figure S.1**

**Verification of the presence of the  $(G_4C_2)_{20}$  or  $(G_4C_2)_{39}$  repeat expansion inside PC12 cells after transfection, and antibiotic selection.** Validation was performed with FISH labeling against  $(G_4C_2)_4$  and subsequent quantification of the average nuclear fluorescent intensity per cell. Bars show the mean value  $\pm$  SEM per condition: non-transfected cells, without FISH labeling (black- representing the cells' intrinsic auto-fluorescence; N=55 for  $(G_4C_2)_{20}$  and N=64 cells for  $(G_4C_2)_{39}$  repeats validation), non-transfected cells, with FISH labeling (yellow- quantifying the non-specific binding of the FISH probes; N=88 for  $(G_4C_2)_{20}$  and N=145 cells for  $(G_4C_2)_{39}$  repeats validation), and cells transfected with either  $(G_4C_2)_{20}$  or  $(G_4C_2)_{39}$ , with FISH labeling (green; N=100 for  $(G_4C_2)_{20}$  and N=166 cells for the  $(G_4C_2)_{39}$  validation). The mean values of the distributions were compared using the Wilcoxon ranksum test. + stands for  $p \leq 0.05$  and \* for  $p < 0.001$ .

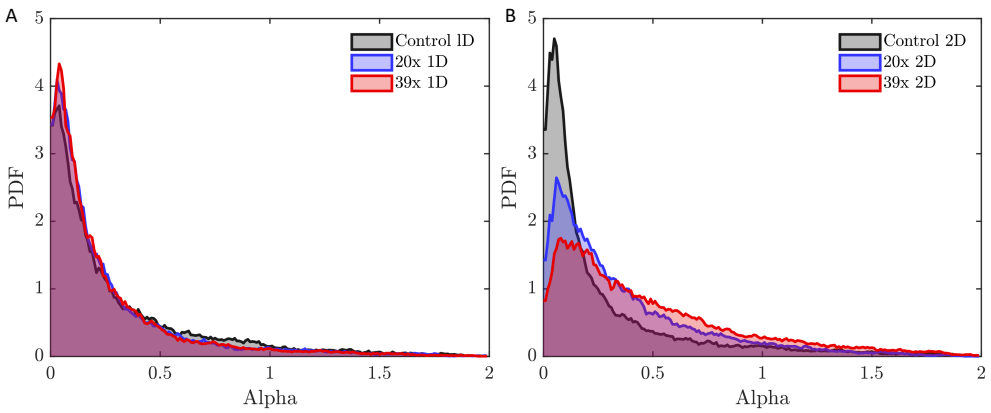


**Figure S.2**

**Probability distribution functions (PDF) of the  $\alpha$  exponent value of lysosomal trajectories.** PDFs of the  $\alpha$  exponent value of lysosomal trajectories inside (A) aligned (1D) and (B) randomly oriented (2D) neurites of differentiated PC12 cells without (control, black) or transfected with the  $G_4C_2$  repeat expansion (( $G_4C_2$ )<sub>20</sub>, blue, and ( $G_4C_2$ )<sub>39</sub>, red, respectively)).

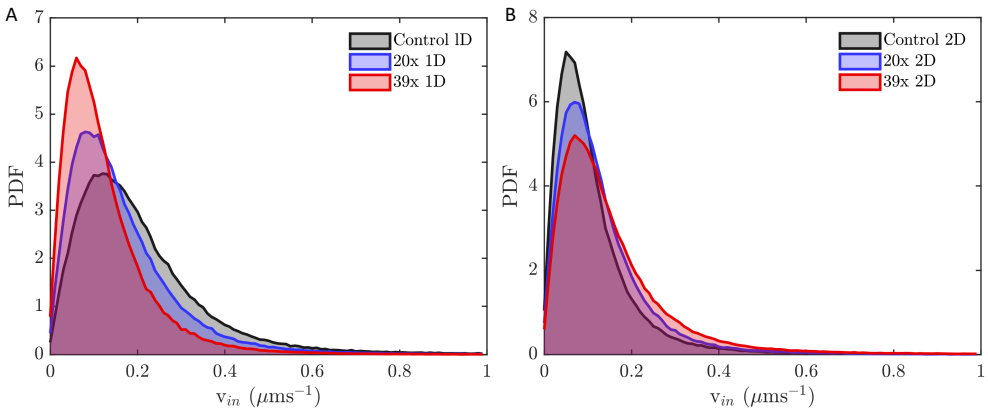


**Figure S.3**

**Probability distribution functions (PDF) of the average instantaneous velocity of lysosomal trajectories shown in Fig. 4.2.** PDFs of the instantaneous velocity of lysosomal trajectories inside (A) aligned (1D) and (B) randomly oriented (2D) neurites of differentiated PC12 cells without (control, black) or transfected with the  $G_4C_2$  repeat expansion (( $G_4C_2$ )<sub>20</sub>, blue, and ( $G_4C_2$ )<sub>39</sub>, red, respectively)).



---

## BIBLIOGRAPHY IV

---

- [1] Stéphanie Millicamps and Jean Pierre Julien. “Axonal transport deficits and neurodegenerative diseases”. In: *Nature Reviews Neuroscience* 14 (3 Mar. 2013), pp. 161–176. ISSN: 1471003X. DOI: 10.1038/nrn3380.
- [2] Scott T. Brady and Gerardo A. Morfini. “Regulation of motor proteins, axonal transport deficits and adult-onset neurodegenerative diseases”. In: *Neurobiology of Disease* 105 (Sept. 2017), pp. 273–282. ISSN: 1095953X. DOI: 10.1016/j.nbd.2017.04.010.
- [3] Li Yu, Yang Chen, and Sharon A. Tooze. “Autophagy pathway: Cellular and molecular mechanisms”. In: *Autophagy* 14.2 (2018), pp. 207–215. DOI: 10.1080/15548627.2017.1378838.
- [4] Hyungsun Park, Ju Hee Kang, and Seongju Lee. “Autophagy in neurodegenerative diseases: A hunter for aggregates”. In: *International Journal of Molecular Sciences* 21 (9 May 2020). ISSN: 14220067. DOI: 10.3390/ijms21093369.
- [5] Pearl P.Y. Lie and Ralph A. Nixon. “Lysosome trafficking and signaling in health and neurodegenerative diseases”. In: *Neurobiology of Disease* 122 (Feb. 2019), pp. 94–105. ISSN: 1095953X. DOI: 10.1016/j.nbd.2018.05.015.
- [6] Dao K.H. Nguyen, Ravi Thombre, and Jiou Wang. “Autophagy as a common pathway in amyotrophic lateral sclerosis”. In: *Neurosci. Lett.* 697.1 (2019), pp. 34–48. DOI: 10.1016/j.neulet.2018.04.006.
- [7] Alan E. Renton et al. “A hexanucleotide repeat expansion in C9ORF72 is the cause of chromosome 9p21-linked ALS-FTD”. In: *Neuron* 72.2 (2011), pp. 257–268. DOI: 10.1016/j.neuron.2011.09.010.
- [8] Mariely DeJesus-Hernandez et al. “Expanded GGGGCC Hexanucleotide Repeat in Noncoding Region of C9ORF72 Causes Chromosome 9p-Linked FTD and ALS”. In: *Neuron* 72.2 (2011), pp. 245–256. DOI: 10.1016/j.neuron.2011.09.011.
- [9] A. Hübers, J. H. Weishaupt, and A. C. Ludolph. “Genetik der amyotrophen Lateralsklerose”. In: *Nervenarzt* 84.10 (2013), pp. 1213–1219. DOI: 10.1007/s00115-013-3898-1.

- [10] Priya Gami et al. “A 30-unit hexanucleotide repeat expansion in C9orf72 induces pathological lesions with dipeptide-repeat proteins and RNA foci, but not TDP-43 inclusions and clinical disease”. In: *Acta Neuropathol.* 130.4 (2015), pp. 599–601. DOI: 10.1007/s00401-015-1473-5.
- [11] Alfredo Iacoangeli et al. “C9orf72 intermediate expansions of 24-30 repeats are associated with ALS”. In: *Acta Neuropathol. Commun.* 7.115 (2019). DOI: 10.1186/s40478-019-0724-4.
- [12] Lieselot Dedeene et al. “An ALS case with 38 (G4C2)-repeats in the C9orf72 gene shows TDP-43 and sparse dipeptide repeat protein pathology”. In: *Acta Neuropathol.* 137.5 (2019), pp. 853–856. DOI: 10.1007/s00401-019-01996-z.
- [13] Mirjana Babić Leko et al. “Molecular mechanisms of neurodegeneration related to C9orf72 hexanucleotide repeat expansion”. In: *Behav. Neurol.* 2019.2909168 (2019). DOI: 10.1155/2019/2909168.
- [14] Estrella Gómez-Tortosa et al. “C9ORF72 hexanucleotide expansions of 20-22 repeats are associated with frontotemporal deterioration”. In: *Neurology* 80.4 (Jan. 2013), pp. 366–370. DOI: 10.1212/WNL.0b013e31827f08ea.
- [15] Julie van der Zee et al. “A Pan-European Study of the C9orf72 Repeat Associated with FTL D: Geographic Prevalence, Genomic Instability, and Intermediate Repeats”. In: *Hum. Mutat.* 34.2 (2013), pp. 363–373. DOI: 10.1002/humu.22244.
- [16] Kaalak Reddy et al. “The disease-associated r(GGGGCC)<sub>n</sub> repeat from the C9orf72 gene forms tract length-dependent uni- and multimolecular RNA G-quadruplex structures”. In: *J. Biol. Chem.* 288.14 (2013), pp. 9860–9866. DOI: 10.1074/jbc.C113.452532.
- [17] Pietro Fratta et al. “C9orf72 hexanucleotide repeat associated with amyotrophic lateral sclerosis and frontotemporal dementia forms RNA G-quadruplexes.” In: *Sci. Rep.* 2 (2012), p. 1016. ISSN: 2045-2322. DOI: 10.1038/srep01016.
- [18] Sarah Mizielinska et al. “C9orf72 frontotemporal lobar degeneration is characterised by frequent neuronal sense and antisense RNA foci”. In: *Acta Neuropathol.* 126.6 (2013), pp. 845–857. DOI: 10.1007/s00401-013-1200-z.
- [19] Zi Fu Wang et al. “The Hairpin Form of r(G4C2)<sub>exp</sub> in c9ALS/FTD Is Repeat-Associated Non-ATG Translated and a Target for Bioactive Small Molecules”. In: *Cell Chem. Biol.* 26.2 (2019), 179–190.e12. DOI: 10.1016/j.chembiol.2018.10.018.

- [20] Tania F. Gendron et al. “Antisense transcripts of the expanded C9ORF72 hexanucleotide repeat form nuclear RNA foci and undergo repeat-associated non-ATG translation in c9FTD/ALS”. In: *Acta Neuropathol.* 126.6 (2013), pp. 829–844. DOI: 10.1007/s00401-013-1192-8.
- [21] Kohji Mori et al. “Bidirectional transcripts of the expanded C9orf72 hexanucleotide repeat are translated into aggregating dipeptide repeat proteins”. In: *Acta Neuropathol.* 126.6 (2013), pp. 881–893. DOI: 10.1007/s00401-013-1189-3.
- [22] Kohji Mori et al. “The C9orf72 GGGGCC Repeat Is Translated into Aggregating Dipeptide-Repeat Proteins in FTL/ALS”. In: *Science (80-. )*. 339.6125 (2013), pp. 1335–1338. DOI: 10.1126/science.1232927.
- [23] Tao Zu et al. “RAN proteins and RNA foci from antisense transcripts in C9ORF72 ALS and frontotemporal dementia”. In: *Proc. Natl. Acad. Sci.* 110.51 (2013), E4968–E4977. DOI: 10.1073/pnas.1315438110.
- [24] Peter E A Ash et al. “Unconventional translation of C9ORF72 GGGGCC expansion generates insoluble polypeptides specific to c9FTD/ALS”. In: *Neuron* 77.4 (2013), pp. 639–646. DOI: 10.1016/j.neuron.2013.02.004.
- [25] Aaron R Haeusler et al. “C9orf72 nucleotide repeat structures initiate molecular cascades of disease”. In: *Nature* 507.7491 (2014), pp. 195–200. DOI: 10.1038/nature13124.
- [26] Ian R A Mackenzie et al. “Quantitative analysis and clinico-pathological correlations of different dipeptide repeat protein pathologies in C9ORF72 mutation carriers”. In: *Acta Neuropathol.* 130.6 (2015), pp. 845–861. DOI: 10.1007/s00401-015-1476-2.
- [27] Brian D. Freibaum and J. Paul Taylor. “The Role of Dipeptide Repeats in C9ORF72-Related ALS-FTD”. In: *Front. Mol. Neurosci.* 10.35 (2017). DOI: 10.3389/fnmol.2017.00035.
- [28] Weilun Pang and Fenghua Hu. “Cellular and physiological functions of C9ORF72 and implications for ALS/FTD”. In: *J. Neurochem.* 157.3 (2020), pp. 334–350. DOI: 10.1111/jnc.15255.
- [29] Jimmy Beckers, Arun Kumar Tharkeshwar, and Philip Van Damme. “C9orf72 ALS-FTD: recent evidence for dysregulation of the autophagy-lysosome pathway at multiple levels”. In: *Autophagy* (2021). DOI: 10.1080/15548627.2021.1872189.
- [30] Yoshitsugu Aoki et al. “C9orf72 and RAB7L1 regulate vesicle trafficking in amyotrophic lateral sclerosis and frontotemporal dementia”. In: *Brain* 140.4 (2017), pp. 887–897. DOI: 10.1093/brain/awx024.

- [31] Sandra Almeida et al. “Modeling key pathological features of frontotemporal dementia with C9ORF72 repeat expansion in iPSC-derived human neurons”. In: *Acta Neuropathol.* 126.3 (2013), pp. 385–399. DOI: 10.1007/s00401-013-1149-y.
- [32] Chantal Sellier et al. “Loss of C9ORF72 impairs autophagy and synergizes with polyQ Ataxin-2 to induce motor neuron dysfunction and cell death”. In: *EMBO J.* 35.12 (2016), pp. 1276–1297. DOI: 10.15252/embj.201593350.
- [33] Janet Ugolino et al. “Loss of C9orf72 Enhances Autophagic Activity via Deregulated mTOR and TFEB Signaling”. In: *PLoS Genet.* 12.11 (2016), e1006443. DOI: 10.1371/journal.pgen.1006443.
- [34] Yon Ju Ji et al. “Systemic deregulation of autophagy upon loss of ALS- and FTD-linked C9orf72”. In: *Autophagy* 13.7 (2017), pp. 1254–1255. DOI: 10.1080/15548627.2017.1299312.
- [35] Christopher P. Cali et al. “C9orf72 intermediate repeats are associated with corticobasal degeneration, increased C9orf72 expression and disruption of autophagy”. In: *Acta Neuropathol.* 138.5 (2019), pp. 795–811. DOI: 10.1007/s00401-019-02045-5.
- [36] Yang Liu and Jiou Wang. “C9orf72-dependent lysosomal functions regulate epigenetic control of autophagy and lipid metabolism”. In: *Autophagy* 15.5 (2019), pp. 913–914. DOI: 10.1080/15548627.2019.1580106.
- [37] Yingxiao Shi et al. “Identification and therapeutic rescue of autophagosome and glutamate receptor defects in C9ORF72 and sporadic ALS neurons”. In: *JCI Insight* 4.15 (2019), e127736. DOI: 10.1172/jci.insight.127736.
- [38] Wan Yun Ho et al. “The ALS-FTD-linked gene product, C9orf72, regulates neuronal morphogenesis via autophagy”. In: *Autophagy* 15.5 (2019), pp. 827–842. DOI: 10.1080/15548627.2019.1569441.
- [39] Manon Boivin et al. “Reduced autophagy upon C9ORF72 loss synergizes with dipeptide repeat protein toxicity in G4C2 repeat expansion disorders”. In: *EMBO J.* 39.e100574 (2020). DOI: 10.15252/embj.2018100574.
- [40] Masin Abo-Rady et al. “Knocking out C9ORF72 Exacerbates Axonal Trafficking Defects Associated with Hexanucleotide Repeat Expansion and Reduces Levels of Heat Shock Proteins”. In: *Stem Cell Reports* 14.3 (2020), pp. 390–405. DOI: 10.1016/j.stemcr.2020.01.010.
- [41] Laura Fumagalli et al. “C9orf72-derived arginine-containing dipeptide repeats associate with axonal transport machinery and impede microtubule-based motility”. In: *Sci. Adv.* 7.15 (2021), eabg3013. DOI: 10.1126/sciadv.abg3013.

- [42] Keertana Venkatesh, Amal Mathew, and Sandhya P. Koushika. “Role of actin in organelle trafficking in neurons”. In: *Cytoskeleton* 77 (3-4 Mar. 2020), pp. 97–109. ISSN: 19493592. DOI: 10.1002/cm.21580.
- [43] Lukas C. Kapitein and Casper C. Hoogenraad. “Which way to go? Cytoskeletal organization and polarized transport in neurons”. In: *Molecular and Cellular Neuroscience* 46 (1 Jan. 2011), pp. 9–20. ISSN: 10447431. DOI: 10.1016/j.mcn.2010.08.015.
- [44] Jeffrey J. Nirschl, Amy E. Ghiretti, and Erika L.F. Holzbaur. “The impact of cytoskeletal organization on the local regulation of neuronal transport”. In: *Nature Reviews Neuroscience* 18 (10 Sept. 2017), pp. 585–597. ISSN: 14710048. DOI: 10.1038/nrn.2017.100.
- [45] Christophe Leterrier, Pankaj Dubey, and Subhojit Roy. “The nano-architecture of the axonal cytoskeleton”. In: *Nat. Rev. Neurosci.* 18 (2017), pp. 713–726. DOI: 10.1038/nrn.2017.129.
- [46] Maria Mytiliniou et al. “Impact of neurite alignment on organelle motion”. In: *bioRxiv* (2021). DOI: 10.1101/2021.07.26.453779.
- [47] Carina Pelzl et al. “Axonal Guidance by Surface Microstructuring for Intracellular Transport Investigations”. In: *ChemPhysChem* 10.16 (2009), pp. 2884–2890. ISSN: 14394235. DOI: 10.1002/cphc.200900555.
- [48] Stephanie May et al. “C9orf72 FTLD/ALS-associated Gly-Ala dipeptide repeat proteins cause neuronal toxicity and Unc119 sequestration”. In: *Acta Neuropathol.* 128.4 (2014), pp. 485–503. DOI: 10.1007/s00401-014-1329-4.
- [49] Matthew D. Cykowski et al. “Dipeptide repeat (DPR) pathology in the skeletal muscle of ALS patients with C9ORF72 repeat expansion”. In: *Acta Neuropathol.* 138.4 (2019), pp. 667–670. DOI: 10.1007/s00401-019-02050-8.
- [50] Yong Jie Zhang et al. “Aggregation-prone c9FTD/ALS poly(GA) RAN-translated proteins cause neurotoxicity by inducing ER stress”. In: *Acta Neuropathol.* 128.4 (2014), pp. 505–524. DOI: 10.1007/s00401-014-1336-5.
- [51] Martin H. Schludi et al. “Spinal poly-GA inclusions in a C9orf72 mouse model trigger motor deficits and inflammation without neuron loss”. In: *Acta Neuropathol.* 134.2 (2017), pp. 241–254. DOI: 10.1007/s00401-017-1711-0.
- [52] Yu Ohki et al. “Glycine-alanine dipeptide repeat protein contributes to toxicity in a zebrafish model of C9orf72 associated neurodegeneration”. In: *Mol. Neurodegener.* 12.6 (2017). DOI: 10.1186/s13024-016-0146-8.

- [53] Shahram Saberi et al. “Sense-encoded poly-GR dipeptide repeat proteins correlate to neurodegeneration and uniquely co-localize with TDP-43 in dendrites of repeat-expanded C9orf72 amyotrophic lateral sclerosis”. In: *Acta Neuropathol.* 135.3 (2017), pp. 459–474. DOI: 10.1007/s00401-017-1793-8.
- [54] Steven Boeynaems et al. “Drosophila screen connects nuclear transport genes to DPR pathology in c9ALS/FTD.” In: *Sci. Rep.* 6 (2016), p. 20877. DOI: 10.1038/srep20877.
- [55] Youn-Bok Lee et al. “C9orf72 poly GA RAN-translated protein plays a key role in amyotrophic lateral sclerosis via aggregation and toxicity”. In: *Hum. Mol. Genet.* 26.24 (2017), pp. 4765–4777. DOI: 10.1093/hmg/ddx350.
- [56] Paige Rudich et al. “Nuclear localized C9orf72-associated arginine-containing dipeptides exhibit age-dependent toxicity in *C. elegans*”. In: *Hum. Mol. Genet.* 26.24 (2017), pp. 4916–4928. DOI: 10.1093/hmg/ddx372.
- [57] Bart Swinnen et al. “A zebrafish model for C9orf72 ALS reveals RNA toxicity as a pathogenic mechanism”. In: *Acta Neuropathol.* 135.3 (2018), pp. 427–443. DOI: 10.1007/s00401-017-1796-5.
- [58] Delphine Arcizet et al. “Temporal analysis of active and passive transport in living cells”. In: *Phys. Rev. Lett.* 101.24 (2008), p. 248103. DOI: 10.1103/PhysRevLett.101.248103.
- [59] Vincent Briane, Myriam Vimond, and Charles Kervrann. “An overview of diffusion models for intracellular dynamics analysis”. In: *Brief. Bioinform.* 21.4 (2019), pp. 1136–1150. DOI: 10.1093/bib/bbz052.
- [60] J. Amick, A. Roczniak-Ferguson, and S. M. Ferguson. “C9orf72 binds SMCR8, localizes to lysosomes, and regulates mTORC1 signaling”. In: *Mol. Biol. Cell* 27.20 (2016), pp. 3040–3051. DOI: 10.1091/mbc.E16-01-0003.
- [61] Peter M. Sullivan et al. “The ALS/FTLD associated protein C9orf72 associates with SMCR8 and WDR41 to regulate the autophagy-lysosome pathway”. In: *Acta Neuropathol. Commun.* 4.51 (2016). DOI: 10.1186/s40478-016-0324-5.
- [62] Mei Yang et al. “A C9ORF72/SMCR8-containing complex regulates ULK1 and plays a dual role in autophagy”. In: *Sci. Adv.* 2.9 (2016), e1601167. DOI: 10.1126/sciadv.1601167.
- [63] Yingying Zhang et al. “The C9orf72-interacting protein Smcr8 is a negative regulator of autoimmunity and lysosomal exocytosis”. In: *Genes Dev.* 32.13-14 (2018), pp. 929–943. DOI: 10.1101/gad.313932.118.

- [64] Qiang Shao et al. “C9orf72 and smcr8 mutant mice reveal MTORC1 activation due to impaired lysosomal degradation and exocytosis”. In: *Autophagy* 16.9 (2020), pp. 1635–1650. DOI: 10.1080/15548627.2019.1703353.
- [65] Dan Tang et al. “Cryo-EM structure of C9ORF72–SMCR8–WDR41 reveals the role as a GAP for Rab8a and Rab11a”. In: *Proc. Natl. Acad. Sci. U. S. A.* 117.18 (2020), pp. 9876–9883. DOI: 10.1073/pnas.2002110117.
- [66] Joseph Amick et al. “PQLC2 recruits the C9orf72 complex to lysosomes in response to cationic amino acid starvation”. In: *J. Cell Biol.* 219.1 (2020), e201906076. DOI: 10.1083/jcb.201906076.
- [67] Christopher P Webster et al. “The C9orf72 protein interacts with Rab1a and the ULK1 complex to regulate initiation of autophagy.” In: *EMBO J.* 35.15 (2016), pp. 1656–76. DOI: 10.15252/embj.201694401.
- [68] Yang Liu et al. “A C9orf72-CARM1 axis regulates lipid metabolism under glucose starvation-induced nutrient stress”. In: *Genes Dev.* 32.21-22 (2018), pp. 1380–1397. DOI: 10.1101/gad.315564.118.
- [69] Mingmei Wang et al. “C9orf72 associates with inactive Rag GTPases and regulates mTORC1-mediated autophagosomal and lysosomal biogenesis”. In: *Aging Cell* 19.e13126 (2020). DOI: 10.1111/ace1.13126.
- [70] Anna Corrionero and H. Robert Horvitz. “A C9orf72 ALS/FTD Ortholog Acts in Endolysosomal Degradation and Lysosomal Homeostasis”. In: *Curr. Biol.* 28.10 (2018), 1522–1535.e5. DOI: 10.1016/j.cub.2018.03.063.
- [71] Longwei Lv et al. “Biomaterial Cues Regulate Epigenetic State and Cell Functions—A Systematic Review”. In: *Tissue Eng. Part B Rev.* 24.2 (2017), pp. 112–132. DOI: 10.1089/ten.teb.2017.0287.
- [72] Sjoerd Van Helvert, Cornelis Storm, and Peter Friedl. “Mechanoreciprocity in cell migration”. In: *Nat. Cell Biol.* 20.1 (2018), pp. 8–20. DOI: 10.1038/s41556-017-0012-0.
- [73] Saurabh S Mogre, Aidan I. Brown, and Elena F. Koslover. “Getting around the cell: Physical transport in the intracellular world”. In: *Phys. Biol.* 17 (2020), p. 061003. DOI: 10.1088/1478-3975/aba5e5.
- [74] Nicholas J. Braun, Dezhi Liao, and Patrick W. Alford. “Orientation of Neurites Influences Severity of Mechanically-Induced Tau Pathology”. In: *Biophys. J.* (2021). DOI: 10.1016/j.bpj.2021.07.011.
- [75] Youn Bok Lee et al. “Hexanucleotide repeats in ALS/FTD form length-dependent RNA foci, sequester RNA binding proteins, and are neurotoxic”. In: *Cell Rep.* 5.5 (2013), pp. 1178–1186. DOI: 10.1016/j.celrep.2013.10.049.

- [76] I Gijssels et al. “The C9orf72 repeat size correlates with onset age of disease, DNA methylation and transcriptional downregulation of the promoter”. In: *Mol. Psychiatry* 21 (2016), pp. 1112–1124. DOI: 10.1038/mp.2015.159.
- [77] Annemarie Hübers et al. “Polymerase chain reaction and Southern blot-based analysis of the C9orf72 hexanucleotide repeat in different motor neuron diseases”. In: *Neurobiol. Aging* 35.5 (2014), 1214.e1–1214.e6. DOI: 10.1016/j.neurobiolaging.2013.11.034.
- [78] Marka van Blitterswijk et al. “Association between repeat sizes and clinical and pathological characteristics in carriers of C9ORF72 repeat expansions (Xpansize-72): A cross-sectional cohort study”. In: *Lancet Neurol.* 12.10 (2013), pp. 978–988. DOI: 10.1016/S1474-4422(13)70210-2.
- [79] Jon Beck et al. “Large C9orf72 hexanucleotide repeat expansions are seen in multiple neurodegenerative syndromes and are more frequent than expected in the UK population”. In: *Am. J. Hum. Genet.* 92.3 (2013), pp. 345–353. DOI: 10.1016/j.ajhg.2013.01.011.
- [80] Angelica Nordin et al. “Extensive size variability of the GGGGCC expansion in C9orf72 in both neuronal and non-neuronal tissues in 18 patients with ALS or FTD”. In: *Hum. Mol. Genet.* 24.11 (2014), pp. 3133–3142. DOI: 10.1093/hmg/ddv064.
- [81] Nanoscribe. *Photonic Professional GT - Nanoscribe*.
- [82] Johannes Schindelin et al. “Fiji: an open-source platform for biological-image analysis”. In: *Nat. Methods* 9.7 (2012), pp. 676–682. ISSN: 1548-7105. DOI: 10.1038/nmeth.2019.
- [83] Jean Yves Tinevez et al. “TrackMate: An open and extensible platform for single-particle tracking”. In: *Methods* 115 (2017), pp. 80–90. DOI: 10.1016/j.ymeth.2016.09.016.